In Hypervelocity Impact, Proceedings of the 2000 Symposium,
International Journal of Impact Engineering, 26: 543-553, 2001.

DAMAGE AND ROCK–VOLATILE MIXTURE EFFECTS ON IMPACT CRATER FORMATION

**JOHN D. O'KEEFE, SARAH T. STEWART,
MICHAEL E. LAINHART AND THOMAS J. AHRENS**

Lindhurst Laboratory of Experimental Geophysics, Seismological Laboratory 252-21
California Institute of Technology, Pasadena, CA 91125

Abstract—We explored simple geologic strength and material response models to determine which have the capability to simulate impact-induced faulting, complicated ejecta patterns and complex crater shapes. This led us to develop models for material damage, dilatancy, and inhomogeneous materials (mixtures). We found that a strength degradation (damage) model was necessary to produce faulting in homogeneous materials. Both normal and thrust ring faults may occur and extend relatively deeply into the planet during the transient cavity radial expansion. The maximum depth of fault development is about the depth of maximum penetration by the projectile. Dilatancy in geologic materials may reduce the final bulk density compared to the pristine state because of irreversible fracturing. When we include the effects of dilatancy, the radial position of faulting is displaced because of greater upward motions. In addition, the late time crater profile is shallower and the expression of features such as central peaks and rings may be more pronounced. Both damage and rock-ice mixtures effect the distribution of ejecta. The excavation flow field within the heavily damaged region is similar to flow fields in Mohr-Coulomb materials with no zero-pressure strength. In the outer, less damaged zone within the excavation cavity, the material trajectories collapse back into the crater. This effect creates a zone of reduced ejecta emplacement near the edge of the final crater. In the case of rock-ice mixtures, energy is preferentially deposited in the more compressible volatile component and the ejecta pattern is dependent upon the location of shock-induced phase changes in the volatile material.

Keywords: impact, shock damage, dilatancy, crater faults, ejecta, thermal fracturing, complex craters.

INTRODUCTION

Faulting, complicated ejecta patterns and crater shape features, e.g. ring structures, are some of the major observable characteristics of impact craters. We have been developing models to calculate the phenomenology associated with impact features [1]. Most of the development of cratering mechanics has focused on hypervelocity impacts between competent rocky bodies. We are interested in how variations in material strength and composition change the crater formation process. We explored simple geologic strength and material response models to determine which have the capability to simulate impact-induced faulting, complicated ejecta patterns and complex crater shapes. This led us to develop models for material damage, dilatancy, and inhomogeneous materials (mixtures). The observable crater measures include the dimensions of flat floors, ring-shaped ridges (which in some cases are fault scarps) and depressions, central peaks and pits. We have related key measures of the cratering process, e.g. transient crater diameter, to the post-

impact crater observables [2,3,4]. In this paper we will discuss simple models for damage, dilatancy, and inhomogeneous materials (mixtures) and show examples of faulting, ejecta distributions and final crater shapes.

DAMAGE AND FAULTING

Our goal was to determine which strength model(s) reproduce the faults and complex features found in large-scale craters. We examined the von Mises and Mohr-Coulomb strength models with and without strength degradation (damage) effects. We modeled damage in geologic materials using a phenomenological approach, which coupled the Johnson-Cook damage model [5] with the geologic strength models in CTH, a three dimensional shock wave physics code [6]. The objective here was not to determine the distribution of fragment sizes, but rather to determine the effect of brecciated and comminuted material on the crater evolution, fault production, ejecta distribution, and final crater morphology. There are a number of definitions of damage, which are discussed in detail by Kachanov [7]. Here, damage is defined as the normalized integrated plastic strain experienced by a given material particle. The time derivative of damage, D, is given by

$$\frac{\mathrm{d}D}{\mathrm{d}t} = \frac{1}{\varepsilon_f}\left(\frac{\mathrm{d}\varepsilon}{\mathrm{d}t}\right), \tag{1}$$

where $\mathrm{d}\varepsilon/\mathrm{d}t$ is the plastic strain rate. The equivalent plastic strain at fracture, ε_f, is defined by

$$\varepsilon_f = \left[A_1 + A_2 e^{-A_3 P/\Psi_0}\right]\left[1 + A_4 \ln f\left(\tfrac{d\varepsilon}{dt}\right)\right]\left[1 + A_5\left(T - T_R\right)/\left(T_M - T_R\right)\right], \tag{2}$$

where $A_1 - A_5$ are material parameters, P and T are the pressure and temperature, and T_M and T_R are the melting temperature and the thermal softening temperature respectively. Ψ_0 is the yield strength at zero pressure, and $f\left(\frac{d\varepsilon}{dt}\right)$ is a function of the strain rate [5]. The degradation in strength is a function of thermal softening, density effects (e.g. extension), and fracturing. The reduction in strength due to fracturing is given by

$$\Psi_d = \Psi_{dT\rho}\left(1 - D\right), \tag{3}$$

where $\Psi_{dT\rho}$ is the thermally and density degraded strength and a function of Ψ_0 [2,6]. The damage function is zero for pristine material and unity at failure. This reduction in strength was incorporated into the geologic strength model to account for pressure effects and is given by

$$\Psi_S = \Psi_{\mathrm{vM}} + \left(\Psi_d - \Psi_{\mathrm{vM}}\right) e^{-A_\Psi P/\left(\Psi_{\mathrm{vM}} - \Psi_d\right)}, \tag{4}$$

where Ψ_{vM} is the limiting strength at high pressure (the von Mises magnitude), and A_Ψ is the tangent of the internal angle of friction.

The yield surface is determined either by the von Mises (independent of P) or Mohr-Coulomb models (Eq. 4) (see Fig. 1). In the case of the von Mises model, the strength drops to zero when the damage is unity and is independent of pressure ($A_\Psi = 0$, zero internal angle of friction). In the case of the Mohr-Coulomb model, the strength at zero confining pressure, Ψ_0, goes to zero as

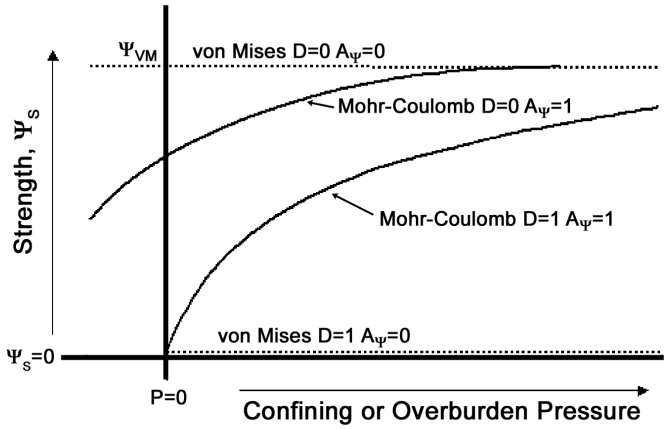

Fig. 1. Schematic of geologic strength models including the effects of damage, *D*.

the damage approaches unity, and the tangent of the internal angle of friction is assumed to be independent of damage ($A_\Psi = 1$). The strength increases with confining pressure to the limiting value of the von Mises amplitude, Ψ_{vM}. The degree of consolidation is measured by the magnitude of the zero pressure yield strength with $\Psi_0 = 0$ representing unconsolidated objects.

Examples of crater profiles for various strength and damage models are shown in Figures 2 and 3. In all of the crater calculation plots, the height *Y* and radial position *r* are normalized by the impactor radius *a*. The time is normalized by *a/U*, where *U* is the impactor velocity. The other dimensionless parameters that characterize the impact conditions [1] are ga/U^2 (inverse Froude number) and $\Psi_{vM}/\rho U^2$ (inverse Cauchy number), where *g* is the object's gravity and ρ is the density.

The collapse number, $\Psi_{vM}/\rho g d_P$, determines the crater formation regime where d_P is the depth of penetration under zero strength conditions. The collapse number is a measure of the material strength at the maximum depth of penetration to the overburden pressure at that depth. When the collapse number is large (>>1), the crater is simple, and when it is small (<<1), the crater is complex. The left side panels in Figs. 2 and 3 show the crater profile and stratigraphy at the time of maximum penetration. In the right side panels, the crater profile and stratigraphy at a later time is superimposed upon the profile at maximum penetration. In order to delineate the effect of the crater motions on the deformation of the planet's stratigraphy via folding and faulting, we have placed Lagrangian tracer particles at various depths. The mechanics of cratering including the evolution of the crater shape, the displacement histories of the stratigraphic profile, and the associated scaling laws are discussed in detail in O'Keefe and Ahrens [1,2]. Fault zones are recognized by examination of the Lagrangian particles for discontinuities in the stratigraphy. The spatial resolution of the particles was about 0.3*a*.

All of the crater profiles shown in Figs. 2 and 3 were calculated for the same impact conditions: $ga/U^2 = 3.4\times10^{-5}$, $\Psi_{vM}/\rho U^2 = 6.2\times10^{-4}$, $\Psi_{vM}/\rho g d_P = 2.0$. In the damage model (Eq. 2), the material parameter $A_1 = 0.1$ and the other damage parameters (A_2-A_5) were assumed to be zero. We chose the value of A_1 as representative of brittle rocks [8]. For this initial study, we are interested in the first order effects of strength degradation, so we ignore any dependence on total stress and strain rate (A_2-A_4). Also, in brittle rocks, one expects a weak dependence on thermal softening (A_5). We have an ongoing effort to develop more detailed models for damage in rocks.

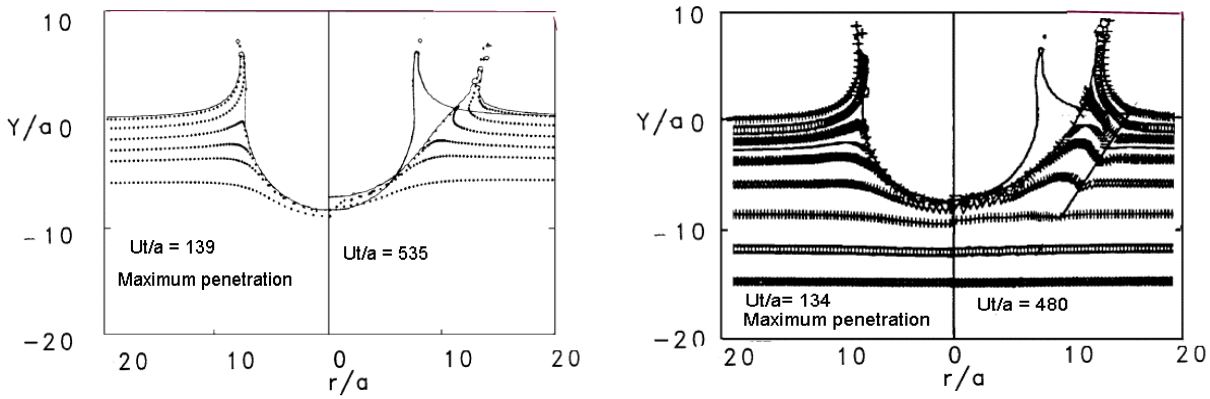

(a) (b)

Fig. 2. Crater profiles at the time of maximum penetration and later during crater collapse. Yield models are (a) Mohr-Coulomb with Ψ_0 =0 and no damage effects and (b) von Mises including damage. (a) Note that faulting did not occur. Final crater has a simple bowl shape. (b) With a damage model, faulting occurs where highlighted on the right panel. Damage fluidizes shocked material and results in a flat-floored final crater shape.

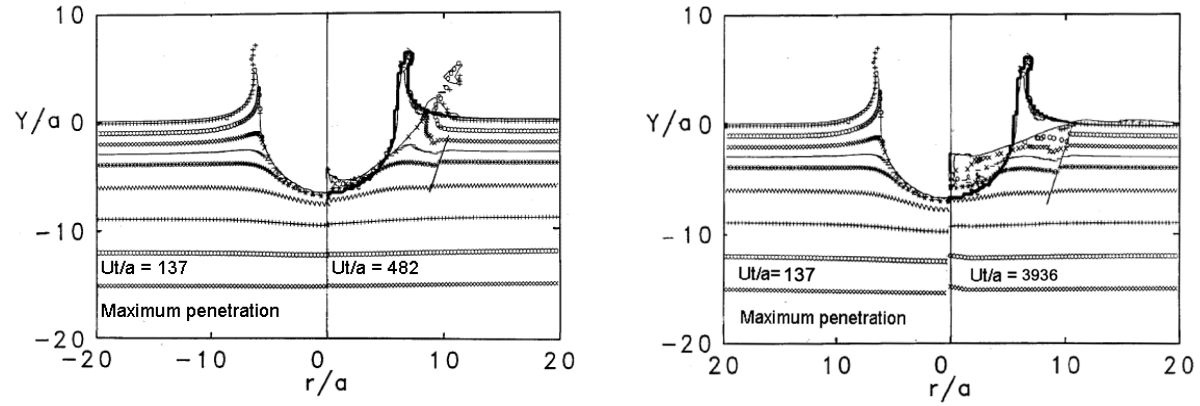

(a) (b)

Fig. 3. Crater profiles at the time of maximum penetration shown on left panel in both (a) and (b). Right panel shows crater profile (a) later during crater collapse and (b) for the final crater shape. The yield model in both (a) and (b) was Mohr-Coulomb with $\Psi_0 = \Psi_{vM}$ and damage effects. Faulting is delineated in the panels on the right. Note multiple faulting in the final crater stratigraphy (b).

We first show a case where the strength model was Mohr-Coulomb with $\Psi_0 = 0$ but without the effects of damage (Fig. 2a). In this case, a standard simple crater forms and the right panel shows the development of the overturned flap of ejecta (c.f. [9]). For both the Mohr-Coulomb and the von Mises models, we did *not* find faulting in the calculations when damage was not included.

The next case uses the von Mises strength model including damage effects (Fig. 2b). Near surface reverse faulting occurred during the radial expansion of the cavity diameter and prior to emplacement of the overturned flap of ejecta. The von Mises model with damage did not give a good representation of the late stage dynamics of the crater formation because of the complete loss of strength in the damaged regions and independence of strength on overburden pressure (zero angle of internal friction). At late times, the damaged material was completely fluidized

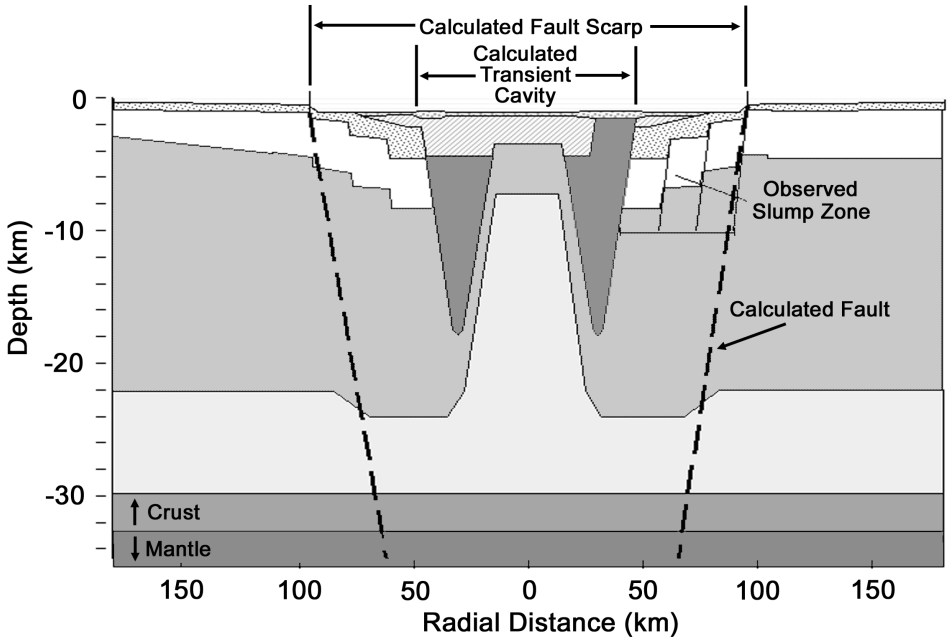

Fig. 4. Chicxulub crater stratigraphy and fault structure as determined from field measurements [11]. The impact parameters and stratigraphy were modeled in O'Keefe and Ahrens [2]. Shown are the calculated fault radius and angle [3]. The depth of fault penetration, ~ 43 km, extends into the mantle.

and sloshed back and forth in a cavity defined by the undamaged material. The turbulent flow in the cavity mixed the stratigraphic layers, which is not observed in the field. The final crater profile was flat-floored with no internal features (rings, central pits, etc.). This situation led us to the Mohr-Coulomb strength model with damage effects.

We found that faulting occurred in homogeneous materials when we implemented a Mohr-Coulomb strength model ($\Psi_0 = \Psi_{vM}$) including damage effects (Fig. 3a). In this case, faulting began early as in the von Mises case with damage. Note that the faulting started relatively deeply into the planet and has not yet propagated to the surface at the normalized time of 482 (right panel Fig. 3a). Fig. 3b shows the same cratering simulation at very late time. By the time the final crater shape formed, the major fault had propagated to the surface and other minor faults developed below the final crater. Note that material in the transient cavity is driven downward during the penetration phase and is subsequently uplifted during the rebound phase. Because of the rebounding effect, the final displacement along the fault decreases with depth. Within the final crater, some of material above the third layer is ejected. Part of the ejecta blanket is shown as an increase in the final surface topography on the far right side of Fig. 3b.

Faulting in geologic materials was shown analytically to be a consequence of strain softening of the yield strength [10]. This effect is simulated by the use of a damage model in the calculations. Damage produces large increments of softening in both the von Mises and Mohr-Coulomb models (Fig.1). Only the Mohr-Coulomb model, however, is realistic for geologic-scale craters. Strain localization is the primary factor in determining the position of faults in the absence of pre-existing damaged regions. In these calculations, the planet's surface composition and strength were initially homogeneous. The damaged zones where faulting occurred evolved naturally during crater formation and were not emplaced *a priori*. The primary faults occurred near the boundary of the damaged zone, in a region where the damage and strength gradients were large.

Circular faults, both normal and reverse, surround craters on the Moon and Venus [9]. On Earth, circular faults have long been recognized around complex craters including the Chicxulub

crater in the Yucatan peninsula. Deep seismic reflection sounding of the Chicxulub crater revealed a ring normal fault that extended from near the surface into the Mohorovičić (Moho) discontinuity, the boundary between the crust and mantle [11,12]. In O'Keefe and Ahrens [2], we were able to match a computer simulation with the stratigraphic profile determined by Hildebrand *et al.* [11] (see Fig. 4). Hence, we could determine the transient cavity radius. From this transient cavity radius and the present faulting calculations, we estimated the Chicxulub fault position and depth of fault penetration.

Our modeling of the Chicxulub stratigraphy and fault position resolves the debate between Chicxulub having a small diameter (~90 km) or large diameter (>180 km) [13] transient cavity. Our calculations predict that for a transient cavity diameter of 90 km, the diameter of the circular fault would be about 180 km in good agreement with field observations (Fig. 4). The corresponding depth of penetration would be 43 km, extending the ring fault down into the Moho discontinuity. In order to model the major aspects of the Chicxulub crater in detail all of the models discussed in this paper would need to be employed in a single simulation. These models include damage to account for faulting, rock-volatile mixture effects to account for the water saturated surface layer and the associated ejecta distribution modifications, and dilatancy to account for any reduction in the density of the bedrock.

DILATANCY AND CRATER SHAPE

Dilatancy has long been recognized as an important aspect of rock response [14]; it is produced by the nucleation and growth of cracks from inhomogeneous stresses during loading. At low peak pressures, dilatancy results in a lower bulk density in the rock. The lower density rock has an important influence on the observable surface features in complex craters (flat floors, rings, central peaks and pits, etc.) and the subsurface damaged zone.

We have developed a simple model for dilatancy that can be readily implemented into hydrocodes and is based on obtainable material properties of the zero pressure end states (Fig. 5). The zero pressure density and the elastic moduli were bounded by the observed properties of competent rock (undamaged rock, D=0.0) and unconsolidated rock (completely damaged rock, D=1.0) [14]. For our initial investigation we have implemented a large dilatancy effect. The slope of the density vs. pressure curve for the consolidated and unconsolidated rock is a function of their measured bulk moduli. For our first-order investigation, we assume that zero-pressure density is linearly proportional to the degree of damage. In addition, the intermediate damage curves are constrained to intersect at the pressure required for complete closure of all cracks. Beyond this point, the material response follows that of consolidated rock. When a material is damaged at low pressures, it unloads along the appropriate pressure-density curve.

The properties of the completely damaged rock shown in the example in Fig. 5 are consistent with the seismic velocities (<1.5 km/s) measured in the damaged region beneath Barringer Crater (Meteor Crater Arizona) [15]. Strength degradation due to the reduced bulk moduli is also accounted for in the model and is inversely proportional to the slopes of the curves in Fig. 5. When we include the effects of dilatancy, the radial position of faulting is displaced because the upward motions produced by decreased density offsets the downward thrusting that produces the deep-seated faulting. In addition, at later times, near surface thrust faulting was found to occur more extensively.

Dilatancy appears to contribute to the development of surface features such as central peaks and rings (Fig. 6). Note that when dilatancy is included, the late time crater profile is shallower because of the lower density of the rock beneath the crater. The percentage change in the centerline height relative to the maximum depth of penetration is 40% for this example, essentially equal to the percentage density difference of the lower density rock at zero pressure.

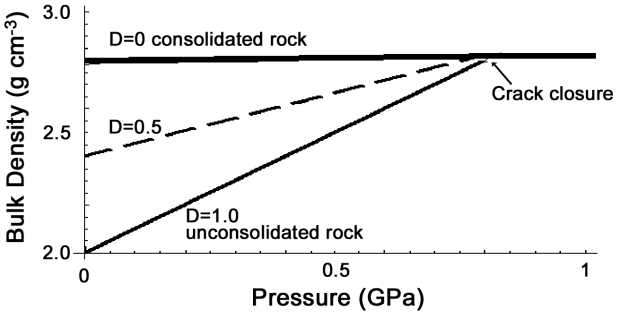

Fig. 5. Simple dilatancy model. The model is constrained at zero pressure by the density and bulk modulus of consolidated rock (D=0) and completely damaged rock (D=1) [14]. Intermediate damage states are assumed to vary linearly in density at zero pressure and intersect the consolidated rock curve at the crack closure stress.

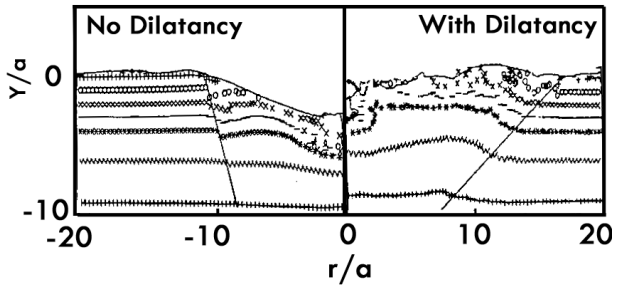

Fig. 6. Final crater profiles showing the effect of dilatancy. The impact parameters are the same as in Figs. 2 and 3. Note that with dilatancy, the final crater shape is shallower as a result of the reduced density of the damaged material [4].

MODIFICATION OF EJECTA DISTRIBUTION

In this section, we consider the major material properties that may contribute to complicated ejecta patterns around craters. Complex ejecta patterns are observed on Earth, e.g. from the Chicxulub crater [16], and on Mars, where some ejecta blankets appear to be layered and fluidized [17]. Here we investigate the effects of damage and ice-rock mixtures on the distribution of ejecta.

Kieffer and Simonds [18] examined 32 of the largest terrestrial impact craters and found that the amount of melt within craters in crystalline rocks is approximately a hundred times greater than within craters in sedimentary rocks. They attributed this discrepancy to the vaporization of volatiles in sedimentary rocks and subsequent acceleration of the melt and rock by expansion of volatiles, which removed more material from within the crater compared to impacts into crystalline rock. In addition, Alvarez *et al.* [16] mapped the ejecta distributions from Chicxulub crater and concluded that volatile expansion played an important role in forming the ejecta distribution. The treatment in these two studies was analytical, and detailed models of mixtures of materials were not yet developed for computer simulations.

Lagrangian codes are inherently unable to handle mixtures of materials. On the other hand, multi-material Eulerian codes, e.g. CTH, in the course of computation are required to handle mixed cells [6]. However, the standard Eulerian codes have not included the ability to accept mixtures of materials as the initial state (input). We have upgraded the Caltech version of CTH to allow an initial mixture of materials. Three general models are available for boundary conditions between components: pressure equilibration with and without thermal equilibrium and variations in pressure.

For bulk mixtures of H_2O and rock, e.g. saturated rock beneath a shallow ocean, the impact temperatures of the components could be very different depending upon the mixture ratio and thermal transport assumption. Table 1 lists the peak shock state in targets composed of H_2O ice, dunite and an ice-dunite mixture subject to a 10 km/s impact by a copper projectile. In this example, we used the CTH library ANEOS version of the equations of state for ice and dunite. The shock states of the rock-ice mixture are assumed to be in pressure but not thermal equilibrium. Note that the peak shock temperature of the ice is substantially higher by almost a

Table 1. Comparison of peak shock states from an impact by a copper projectile at 10 km/s. The 50/50 by volume ice-rock mixture case forced pressure equilibrium between the components but allowed thermal disequilibrium. Initial temperature in each case was 200 K.

Case	*Component*	*Unshocked Density (Mg/m^3)*	*Component Density (Mg/m^3)*	*Shock Pressure (GPa)*	*Shock Density (Mg/m^3)*	*Shock Temperature (K)*
Ice Only	Ice	0.919		97	2.14	8,800
Rock Only	Dunite	3.32		266	5.9	8,540
Ice-Rock Mixture	Mixture	2.119		185	4.21	
	Ice		0.919		2.39	23,500
	Dunite		3.32		5.33	7,980

factor of three in the mixture configuration compared to the pure ice target. The higher temperature in the H_2O is a result of the larger compressibility of H_2O compared to dunite, which deposits a greater proportion of the total PdV work into the H_2O component.

We also modeled penetration of high-density probes into porous rock-ice mixtures that are representative of comets [19]. Using a mixture of materials gives the capability to easily model a variety of geologic materials without developing a new equation of state for each new composition (recipe) of individual components. We can also impose boundary conditions appropriate for different geologic situations. For example, if the material in comets were mixed on a very fine scale, the components of the mixture would probably satisfy both pressure and thermal equilibrium.

Both damage and rock-volatile mixtures influence the ejecta distributions. Figure 7 shows examples of ejecta distributions for targets with (a) no strength, (b) Mohr-Coulomb strength and no damage effects, (c) Mohr-Coulomb strength including damage effects, and (d) a rock-ice composition and Mohr-Coulomb strength with no damage effects. The Lagrangian particle trajectory histories are shown for those particles that are ejected to positions above the initial surface. This defines the region that is known as the excavation cavity [2,9].

First consider the ejecta trajectories for an impact on a strengthless object (Poisson ratio is 0.5) with zero gravity (Fig. 7a). The ejecta trajectories are very linear away from the impact point and are essentially ballistic starting at positions within the excavation cavity. Because of the absence of gravity, the particle trajectories do not turn over. The ejection angle is initially very steep and steepens further at distances away from the impact point, approaching 90^o from the horizontal. This is the value predicted by Melosh [20] for materials with a Poisson ratio of 0.5 and observed for impacts into water [21]. The difference in ejection angle near the impact point is probably related to the finite size of the projectile. The ejecta scaling laws developed by Housen *et al.* [22] assume that at distances away from the impact point, the ejection angles are constant and do not vary with radial position. This assumption is valid for hydrodynamic materials.

Next, we show the ejecta trajectories for an impact on an object obeying a Mohr-Coulomb strength model with Poisson ratio of 0.35 and no damage effects (Fig. 7b). The impact parameters are the same as in Figs. 2 and 3. In this case, the yield strength at zero pressure is zero ($\Psi_0 = 0$). There appears to be a near-surface effect that alters the trajectories of the particles in the top layer. The trajectories for these particles, originally located just below the boundary layer, are initially steep and bend slightly at positions above the initial surface level. We infer that there are hydrodynamic interactions that occur above the initial surface level and turn the flow. The final location of the ejecta from this zone is determined by the ballistic trajectory angle after this interaction, not the ejection angle at the initial surface. We are investigating possible

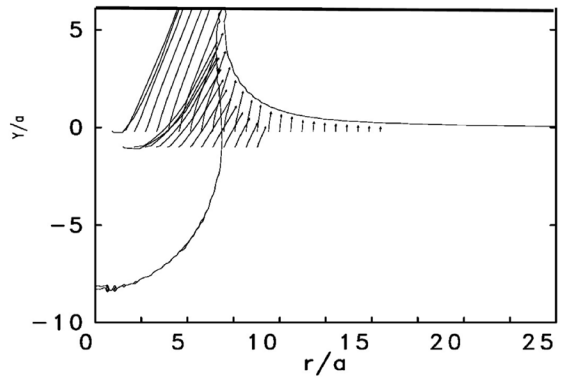

Fig. 7a. Ejecta trajectories for a hydrodynamic material. The material has zero strength, Poisson ratio of 0.5, and no gravity. $Ut/a = 107$.

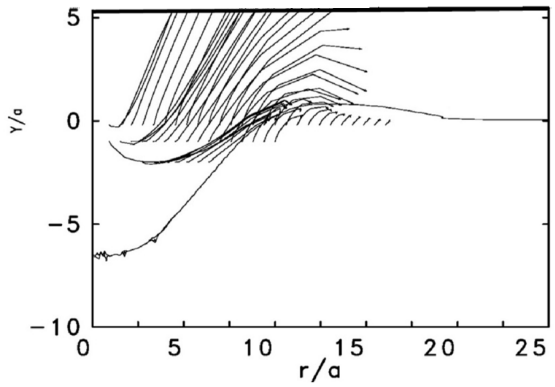

Fig. 7b. Ejecta trajectories for a Mohr-Coulomb strength model with $\Psi_0 = 0$ and no damage effects. The impact parameters are the same as in Figs. 2 and 3. $Ut/a = 1473$.

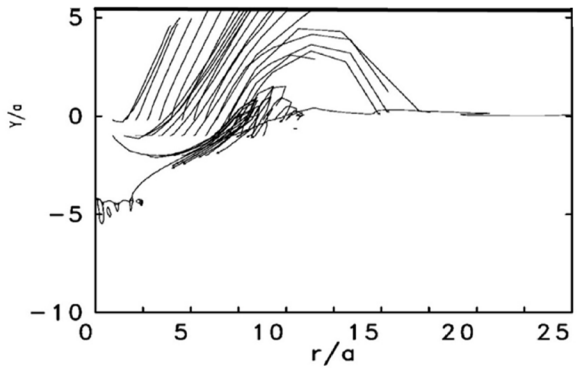

Fig. 7c. Ejecta trajectories for a Mohr-Coulomb strength model with $\Psi_0 = \Psi_{vM}$ including damage effects. The impact parameters are the same as in Figs. 2 and 3. $Ut/a = 981$.

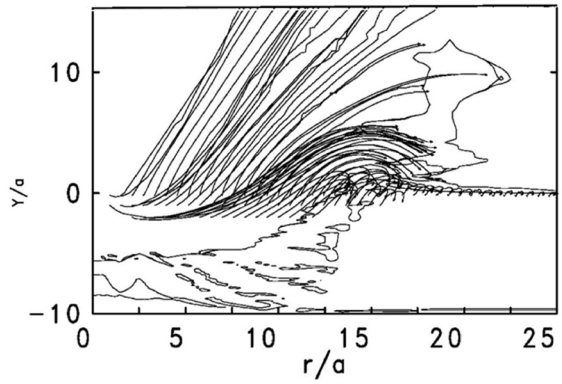

Fig. 7d. Ejecta trajectories for an impact on a rock-ice mixture showing the effects of inhomogeneous shock heating and hydrothermal fracturing [24]. $Ut/a = 1220$. See text for impact parameters.

physical processes that may be the cause this change in the flow streams, which would be an important modification of simple crater ejecta models such as the Maxwell Z-model [23].

When we include the effects of damage, the ejecta trajectories can be significantly altered. Fig. 7c shows the ejecta trajectories for an impact on an object under the same conditions as in Fig. 7b but with damage included in the strength model and $\Psi_0 = \Psi_{vM}$. The material within the radial position, $r/a < 7$ is heavily damaged. The primary effect of damage on the ejecta is the reduction of the strength of the material within the excavation cavity. Because we assumed that the fully damaged material obeyed a Mohr-Coulomb strength model with $\Psi_0 = 0$, the response of the material within the damaged zone was the same as the initial condition for the case shown in Fig. 7b where we used a Mohr-Coulomb model with no damage and an initial $\Psi_0 = 0$. The ejecta trajectories in the fully damaged region in Fig. 7c are very similar to those in the same zone in Fig. 7b. However, the ejecta trajectories outside the heavily damaged region are very different. The material from this zone does not escape the crater cavity; instead it collapses back into the crater. The lack of particle trajectories landing just outside the crater rim (Fig. 7c) implies that

this zone will have less material in the ejecta blanket. The final crater shape in Fig. 3b shows that the ejecta blanket thickness is smaller nearer the crater rim compared to farther away.

The ejection trajectories are also affected by the heterogeneous response of rock-ice mixtures. The ejecta distributions around Chicxulub crater and fluidized ejecta blankets on Mars can be explained by the presence of a rock-volatile mixture in the upper stratigraphic layer. We present the ejecta trajectories for a 1-km diameter dunite projectile impact on the Martian surface (Fig. 7d). The surface gravity was 3.7 m s^{-2} and the impact velocity was 10 km/s. The upper 5 km of the Martian surface was modeled as a 15 vol% ice–85 vol% dunite mixture over a pure dunite substrate [24]. The zero pressure strength of the Martian regolith-ice mixture was assumed to be small, Y_0 = 10 MPa, and we used a Mohr-Coulomb strength model with A_Y = 1. The impact parameters were $ga/U^2 = 1.85\times10^{-5}$, $Y_{vM}/\rho U^2 = 3.5\times10^{-5}$, $Y_{vM}/\rho g d_P = 0.3$.

The ice and rock components of the mixture were constrained to be in pressure equilibrium but allowed thermal disequilibrium. Since ice is more compressible than rock, more work was done on the ice and a larger volume was subjected to shock-induced phase transformations compared to the rock. In this impact situation, a small zone of rock is melted (~1*a*) and very little is vaporized. The rest of the rock within the excavation cavity does not undergo any major phase transitions. The zone of ice that is vaporized is about 1*a* and the melted zone is about 7*a* for these impact conditions. From about 1-7*a*, the material state during the excavation is a mixture of water and comminuted rock. Within this zone the ejection angles are all very steep, about 70°, decreasing with increasing distance from the impact point to about 45° near the crater rim (Fig. 7d). There is a clear separation in the ejecta trajectories at about 7*a*. This modification in the ejection angles is related to the difference in strength of the heterogeneous materials within the excavation cavity. The final ejecta blanket will contain a significant amount of liquid water allowing for fluidized flow [24].

Another interesting feature found to occur in the modeling of rock-ice mixtures was hydrothermal fracturing of the cavity region (Fig. 7d). Fracturing is not observed without a damage model or a mixture of materials (e.g. Figs. 7a and 7b). For rock-volatile mixtures, the heterogeneous compression and release of the individual components generates fractures around the transient cavity.

CONCLUSIONS

We implemented simple geologic strength and material response models to simulate impact-induced faulting, complicated ejecta patterns and complex crater shapes. We found that material damage, dilatancy, and material mixtures have a significant effect on crater formation processes. We found that a strength degradation (damage) model was necessary to produce faulting in homogeneous materials. Dilatancy in geologic materials may displace the location of impact-induced faulting and change the final crater shape. Both damage and rock-ice mixtures effect the distribution of ejecta. In the case of rock-ice mixtures, energy is preferentially deposited in the more compressible volatile component and the ejecta pattern is dependent upon the location of shock-induced phase changes in the volatile material.

Acknowledgement—We thank the reviewers for their thoughtful comments. In addition we appreciate the readily given assistance of Gene Hertel of Sandia Laboratories in the use of CTH. This research was supported under NASA/Goddard grant NAG5-8915. Contribution number 8714, Division of Geological and Planetary Sciences, California Institute of Technology, Pasadena, CA 91125.

REFERENCES

[1] O'Keefe JD, Ahrens TJ. Planetary cratering mechanics. *J. Geophys. Res*., 1993; **98**(E9): 17,011-17,028.

[2] O'Keefe JD, Ahrens TJ. Complex craters: Relationship of stratigraphy and rings to the impact conditions. *J. Geophys. Res*., 1999; **104**(E11): 27,091-27,104.

[3] O'Keefe JD, Ahrens TJ. Deep seated faulting in the formation of complex craters. *Lunar Planet. Sci. Conf*., Vol. 30, Houston, TX, 1999: Abstract 1304.

[4] O'Keefe JD, Ahrens TJ. Impact bulking, faulting and ejecta. *Lunar Planet. Sci. Conf*., Vol. 31, Houston, TX, 2000: Abstract 1429.

[5] Johnson GR, Holmquist TJ. An improved computational model for brittle materials. In: Schmidt SC, Shaner JW, Samara GA, Ross M, editors, *High-Pressure Science and Technology - 1993*, AIP Press, Woodbury, NY, 1994. p. 981-984.

[6] McGlaun JM, Thomson SL. CTH: A Three-dimensional shock wave physics code. *Int. J. Impact Eng.*, 1990; **10**: 360-361.

[7] Kachanov LM. *Introduction to Continuum Damage Mechanics*, M. Nijhoff, Dordrecht, The Netherlands, 1986.

[8] Jaeger JC, Cook NGW. *Fundamentals of Rock Mechanics*, Chapman and Hall, 3rd edition, 1979.

[9] Melosh HJ. *Impact Cratering: A Geologic Process*, Oxford UP, New York, 1989.

[10] Rudicki JW, Rice JR. Conditions for the localization of deformation in pressure-sensitive dilatant materials. *J. Mech. Solids*, 1975; **23**: 371-394.

[11] Hildebrand AR, Pilkington M, Ortiz-Aleman C, Chavez R, Urrutia-Fucugauchi J, Connors M, Graniel-Castro E, Camara-Zi A, Halpenny J, Niehaus D. Mapping Chicxulub crater structure with gravity and seismic reflection data. In: Grady MM, Hutchinson R, McHall GJH, Rothery DA, editors, *Meteorites: Flux with time and impact effects*, Geological Society, London, 1998. p. 177-193.

[12] Morgan J, Warner M, Chicxulub Working Group, Brittan J, Buffler R, Camargo A, Christeson G, Denton P, Hildebrand A, Hobbs R, Macintyre H, Mackenzie G, Maguire P, Marin L, Nakamura Y, Pilkington M, Sharpton V, Snyder D, Suarez G, Trejo A. Size and morphology and the Chicxulub impact crater. *Nature*, 1997; **390**: 472-476.

[13] Sharpton VL, Burke K, Camargo-Zanoguera A, Hall SA, Lee DS, Marin LE, Suárez-Reynoso G, Quezada-Muñeton JM, Spudis PD, Urrutia-Fucugauchi J. Chicxulub multi-ring impact basin - size and other characteristics derived from gravity analysis. *Science*, 1993; **261**: 1564-1567.

[14] Brace WF, Paulding Jr. BW, Scholz C. Dilatancy in the fracture of crystalline rocks. *J. Geophys. Res.*, 1966; **71**: 3939-3953.

[15] Ackerman HD, Godson RH, Watkins JS. A seismic refraction technique used for subsurface investigations at Meteor Crater, Arizona. *J. Geophys. Res.*, 1975; **80**: 765-775.

[16] Alvarez W, Claeys P, Kieffer SW. Emplacement of Cretaceous-Tertiary boundary shocked quartz from Chicxulub Crater. *Science*, 1995; **269**: 930--934.

[17] Carr MH, Crumpler LS, Cutts JA, Greeley R, Guest JE, Masursky H. Martian impact craters and emplacement of the ejecta by surface flow. *J. Geophys. Res.*, 1977; **82**(28): 4055-4065.

[18] Kieffer SW, Simonds CH. The role of volatiles and lithology in the impact cratering process. *Rev. Geophys. Space Phys.*, 1980; **18**: 143-181.

[19] O'Keefe JD, Stewart ST, Ahrens TJ. Impacts on comets and asteroids. *Bull. of the American Astronomical Soc.*, Vol. 32 No. 2, 2000. p. 999.

[20] Melosh HJ. Impact Ejection, Spallation, and the origin of meteorites. *Icarus*, 1984; **59**: 234-260.

[21] Gault DE, Greeley R. Exploratory experiments of impact craters formed in viscous-liquid targets: Analogs for Martian rampart craters? *Icarus*, 1978; **34**: 486-495.

[22] Housen KR, Schmidt RM, Holsapple KA. Crater ejecta scaling laws: Fundamental forms based upon dimensional analysis, *J. Geophys. Res.*, 1983; **88**: 2485-2499.

[23] Maxwell DE. Simple Z model of cratering, ejection and the overturned flap. In: Roddy DJ, Pepin RO, Merrill RB, editors, *Impact and Explosion Cratering*, Pergamon Press, New York, 1977. p. 1003-1008.

[24] Stewart ST, O'Keefe JD, Ahrens TJ. The role of subsurface ice in rampart crater formation. *Bull. of the American Astronomical Soc.*, Vol. 32 No. 2, 2000. p. 1112.